Journal of Operation and Automation in Power Engineering

Vol. XX, No. XX, Dec. 2022, Pages: XXXX (Proofed)

http://joape.uma.ac.ir

*Research Paper*

# SSR Mitigation with a High Power PV Farm Based on Optimal Damping Controller Placement in Active and Reactive Control Loops

*Mahsa Khayyatzadeh* and *Rasool Kazemzadeh* *

*Faculty of Electrical Engineering, Sahand University of Technology, Tabriz, Iran.*

***Abstract***— *With the rapid increase in high penetration photovoltaic (PV) power generation systems into power systems around the world, the idea of power system oscillation mitigation with auxiliary control of PV plant has been suggested recently. In this study, the optimal control of a high penetration PV solar farm in sub-synchronous resonance (SSR) mitigation will be explored. The main contribution of the paper is designing a conventional sub-synchronous resonance damping controller (SSRDC) by properly choosing the best place in the active and reactive controllers of PV farm to place the sub-synchronous damping controller to achieve the best damping in various conditions. Also, the paper presents a complete dynamic model tailored to study via eigenvalue analysis, SSR events in the presence of a high penetration PV farm, and a systematic procedure to design a damping controller using Whale Optimization Algorithm (WOA). The results are validated through two case studies based on the IEEE first and second benchmark model for sub-synchronous resonance studies in MATLAB/Simulink and the achieved numerical results are thoroughly discussed.*

***Keywords***—Sub-synchronous resonance, whale optimization algorithm, photovoltaic power, control loop.

## NOMENCLATURE

| | |
|---|---|
| $C_2$ | Temperature coefficient of the cell temperature |
| $C_r$ | Zero-sequence reference voltage |
| $C_t$ | The voltage of the inverter to the PCC(V) |
| $HP$ | High pressure turbine shafts |
| $I_t$ | Temperature coefficient of the short circuit current |
| $I^m_{sc,\,o}$ | Short circuit current |
| $I^m_{sc,\theta}$ | Short circuit current of the module |
| $IP$ | Intermediate pressure turbine |
| $LPB$, $LPA$ | Low pressure turbine |
| $N_{pm}$ | The number of parallel cells in the module |
| $N_{sm}$ | The number of series cells in the module |
| $p^m_{\max,\,0}$ | Maximum power |
| $P^m_{\max,o}$ | Maximum power of the module |
| $T_{HP,IP}$ | The torque between intermediate and high pressure turbines |
| $T_{IP,LPA}$ | The active reference power(W) |
| $T_{LPA,LPB}$ | The circuit maximum tolerable passing current (A) |
| $V_{MPP}$ | Voltage of MPPT of the module in standard conditions |
| $V^m_{oc,\,o}$ | Open circuit voltage |
| $V^m_{oc.0}$ | Open circuit voltage of the module |
| $I_{MPP}$ | Current of MPPT of the module in standard conditions |

Received: 13 Sep. 2023
Revised: 30 Jan. 2024
Accepted: 11 Jul. 2024
*Corresponding author:
E-mail: r.kazemzadeh@sut.ac.ir (R. Kazemzadeh)
DOI: 10.22098/joape.2024.13109.2009



## 1. INTRODUCTION

In recent years, by the growth in the renewable power generation systems, the installed capacity is an important driving factor in the movement towards smart electric power systems. Wind, tidal and photovoltaic (PV) power generation systems are the promising power sources and a large number of high penetration PV, tidal and wind farms have been installed worldwide. With increasing installation of high penetration PV and wind farms, the auxiliary control of these systems to power system oscillation damping has been suggested. Several researches have been conducted focusing on the impact of wind, tidal and PV farms on different categories of stability such as inter-area oscillation damping [1–3] and Sub-Synchronous Resonance (SSR) damping [4]. Ref. [1] presents a data-centric model prophetic control for supplemental control of a Doubly-Fed Induction Generator (DFIG)-based wind farm to improve the stability of power systems. In [2] an output-feedback $H\infty$ robust criterion has been proposed to design a damping controller for a high penetration photovoltaic farm towards mitigating low frequency swings of power systems. Ref. [3] determined the impressiveness of efficiency a Teaching-Learning-Based-Optimization (TLBO) based on conventional damping controller at a DFIG based tidal power plant to prosperously mitigate the inter-area oscillations arisen from an interconnected power system. In [4], a new method for damping SSR fluctuations in power systems including DFIG-based wind farms linked to series capacitive compensated transmission lines has been presented.

It is well known that one of the fundamental issues in designing damping controllers for various devices such as Flexible AC Transmission Systems (FACTS) devices, DFIG based wind farms, and High Voltage Direct Current (HVDC) systems is the selection of proper point for applying damping controller output signal for oscillation mitigation. The selection of an appropriate control loop and the choice of a suitable point for inserting damping controller signal can greatly increase damping performance of designed damping controllers [5]. To achieve this end, several studies have recently been conducted focusing on determining the best control loop and the best point of Doubly-Fed Induction Generator (DFIG) based wind farm control systems to apply damping controller effect [6, 7]. For example, in [6] a proper technique to identify the best input controlling signal location pair for supplementary damping controller for DFIG, based on the right half-plane zero method, relative gain array method, and Henkel singular value is proposed. Ref. [7] studies SSR damping with DFIG based wind farms focusing on the choice of a proper point on DFIG rotor and grid side converter controllers for applying damping controller output signal. In addition to the widespread application of high power wind farms to power system oscillation damping, worldwide application of high penetration PV farms to power system oscillation damping is growing rapidly in recent years [2] and [8–10]. For example Ref. [10] presents a novel control of PV solar farm as a STATCOM (PV-STATCOM) coordinated with Power System Stabilizers (PSSs) for damping of electromechanical oscillations in a power system.

The SSR mitigating using large-scale PV farms has also been studied by our recent paper in [11] and with Varma et. all in [12]. Our goal in [11] was designing an auxiliary SSRDC for a PV plant to increase the stability of SSR modes in various cases such as PV plant size and power system configuration changing. In both papers [11, 12] only the simulation models are used for validation and only one point of PV plant in reactive power control loop is examined.

Although many aspects of designing damping controllers and determining the best control loop and the best point of the wind farm control system for applying damping controller are investigated in the literature, for PV farms, designing the damping controllers and determining the best control loop and the best point to apply damping controllers signals have not been given enough attention. So, the main contribution of the paper is designing a conventional damping controller on a high power PV plant for SSR mitigation focusing on determining the appropriate control loop and selecting the proper point for employing damping controller. Several possible points of the PV plant active and reactive control loops where the SSR damping controller (SSRDC) can be introduced are studied and the optimum points are identified. Both simulation model and modal analysis (eigenvalue analysis) are performed for a high penetration PV plant aggregated with a series compensated electric power system in MATLAB/Simulink. A new algorithm of optimization with the name of Whale Optimization Algorithm (WOA) for running the optimization problems has been applied. The results have been accredited through two case studies of the IEEE first and second benchmark models. Through using performance index (PI), which describes focusing on the power system dynamics and time-domain simulations, it is proved that the photovoltaic farm reactive power control loop is the best place to insert the SSRDC.

The rest of the paper is outlined as follows. Section 2 demonstrates the IEEE first and second benchmark systems modeling for eigenvalue analysis. Section 3 introduces Whale Optimization Algorithm method and Section 4 explains SSR damping controller design with this algorithm. In Section 5, the simulation results and eigenvalues analysis for both case studies are presented. Section 6 presents the Performance Index analysis. The paper is concluded in Section 7.

## 2. System modelling for eigenvalue analysis

To figure out the validation of the suggested scheme, the IEEE first and second benchmark models for computer simulation of sub-synchronous resonance are displayed (see Fig. 1) and defined as systems I and II, respectively and extracted as test systems [13, 14]. The system I inclusive of 892.4 MVA turbine generator is connected to the infinite bus by a radial series-compensated line. The frequency is 60 Hz. and the rated voltage is 539 kV. The mechanical system is consist of a four step steam turbine, the generator and a rotating exciter. In system II, a single generator of 600 MVA, 22 kV is connected to the infinite bus by two parallel transmission lines. One of the lines is compensated by the series capacitor. Also, the mechanical system includes two stage steam turbines, the generator, and rotating exciter.

In both systems, the 90 MW PV farm is joined to the system at bus 1 (shown in Fig. 1). In other words, in system I, the photovoltaic plant influence is adapted to give about 10% of the formal power of generator and in system II, the photovoltaic plant influence is adapted to give 15% of the formal power of generator.

The PV plants are connected to bus 1 with a 20 km line to introduce active/reactive power to the systems. Collection of collector system can be done by the NREL equivalency method [15]. It is clear that the impact of a photovoltaic farm on dynamic of power system is minimum while placed in miniature size. But, while influence rate rises, the power system dynamic performance can be notably affected [2] and [8–12]. However, according to the high influence of photovoltaic farms that have been installed worldwide (such as plants in Ontario (100 MW) in Canada, Briest (91 MW) in Germany, Montalto di Castro (84.2 MW) in Italy, Lopburi (73 MW) in Thailand, and so on), in this paper a 90 MW PV plant is considered for the study of proposed idea. In the following section, the linearized models of all parts of test system are extracted and then they are added altogether for eigenvalue analysis. In the following, linearized model of PV plant is derived and finally, we have compared the results of eigenvalue analysis in the cases of with and without PV plant. Due to the space limitation, the linearized model just for system I is obtained and presented. But, for time-domain simulations both systems are studied and more focus will be on system II.

### 2.1. Combined generator and shaft system model

In literature, many articles have been published about linearized model of generator and shaft systems for IEEE-FBM [16, 17]. In the same manner as shown in [16], the equations that linearized state are presented by:

$$\Delta \dot{X}_G = [A_G]\Delta X_G + [B_G]\Delta u_G \tag{1}$$

$$\Delta y_G = [C_G]\Delta X_G \tag{2}$$

Where the state vector, input vector and output vector are presented respectively as below:

$$\begin{aligned} &X_G^T = \\ &\Big[\psi_d \psi_q E'_d E'_q \delta_g S_e T_{g,e} S_g T_{LPB,g} S_{LPB} \\ &T_{LPA,\ LPB} S_{LPA} T_{IP,LPA} S_{IP} T_{HP,IP} S_{HP}\Big] \end{aligned}$$

$$u_G^T = [v_D\ v_Q] \ \text{ And } y_G^T = [i_{LD}\ i_{LQ}] \tag{3}$$

Where $\psi$ shows the stator flux linkage, $\acute{E}$ shows the transient internal voltage, $\delta_g$ denotes the rotor angle, $S$ is the per-unit slip and $T$ shows the torque. Pay attention that the mechanical systems with six masses contain the generator (g), exciter (e), low pressure turbine (LPB, LPA), intermediate pressure turbine (IP), and high pressure (HP) turbine shafts. The torques among the shaft masses are specified by subscripts. The terminal voltages is input vector and the output one is the armature currents. that the generator electrical quantities are represented in d–q domain with relation to the synchronously rotating frame of the generator. The input and output quantities, although, are transformed with regard to a common reference frame for the whole system.

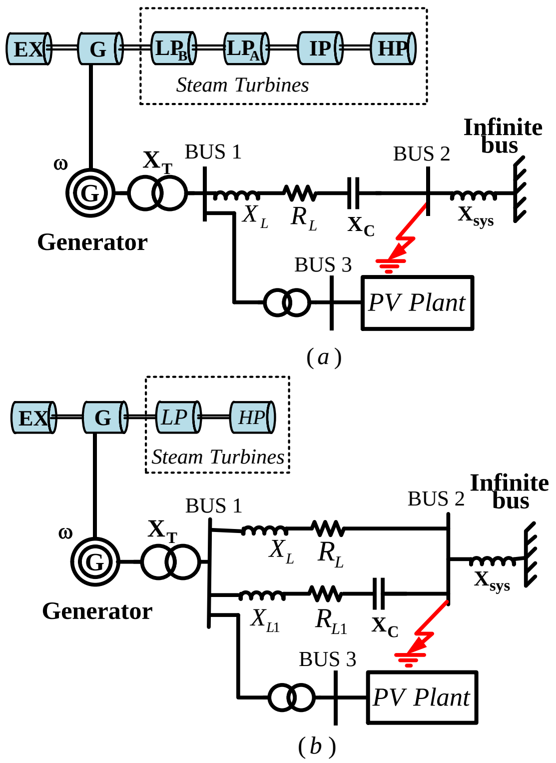


Fig. 1. Test systems schematic design. (a) Systems I (b) Systems II.

### 2.2. Model of the network

For a network with two ports, while one point is connected to an infinite bus, linearized equations could be shown as below [17]:

$$\Delta \dot{X}_N = [A_N]\Delta X_N + [B_N]\Delta u_N \tag{4}$$

$$\Delta u_G = \frac{X_T}{\omega}\Delta \dot{y}_G + [F]\Delta y_G + [F_S]\Delta X_N \tag{5}$$

The matrices $A_N$, $B_N$, $F$ and $F_S$ will be different for different series plans of compensation. At the moment, we proposed them for the two compensation schemes reminder above.

#### A) Fixed series capacitor compensation

In order to fixed series we pick out [16]:

$$\Delta X_N^T = [\Delta V_{cD}\ \Delta V_{cQ}] \text{ And } \Delta u_N^T = [\Delta i_{LD} \Delta\ i_{LQ}] \tag{6}$$

$$A_N = \begin{bmatrix} 0 & -\omega \\ \omega & 0 \end{bmatrix},\ B_N = \begin{bmatrix} \omega X_C & 0 \\ 0 & \omega X_C \end{bmatrix}$$

$$F = \begin{bmatrix} R & X_T \\ -X_T & R \end{bmatrix} \ And\ F_S = \begin{bmatrix} 1 & 0 \\ 0 & 1 \end{bmatrix} \tag{7}$$

Where $X_C$ is the value of the fixed series capacitor and $X_T = (L_1 + L_2).\omega$. Also $V_{cD}$ and $V_{cQ}$ are the D–Q capacitor voltage components.

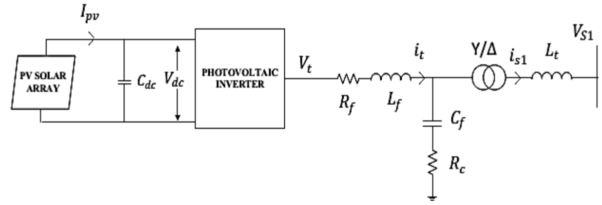


Fig. 2. Grid-connected circuit model of photovoltaic plant.

#### B) Photovoltaic model

The suggested configuration of the photovoltaic plant is illustrated in Fig. 2, is link to the DC side of a three-phase DC-AC Voltage Source Inverter (VSI) [18, 19].

The output current of the PV array according to an exponential function and physics of the PN joint is considered as Eq. (8).

$$I_{pv} = I_{sc}\left[1 - \exp\left(\frac{V - V_{oc} + I\,R_s}{V_t}\right)\right] \tag{8}$$

And the open circuit voltage is given by Eq. (9):

$$V_{oc} = N_{sm}.V_{oc}^c \tag{9}$$

Furthermore, the equivalent parallel resistance of the module is calculated as:

$$R_s = \frac{N_s}{N_p}.R_s^c \tag{10}$$

Thermal equivalent voltage in a PV module is expressed as Eq. (11):

$$V_t = N_s.V_t^c = N_s\frac{mkT^c}{e} \tag{11}$$

The equation of the input DC voltage and output AC voltage of the VSI is shown below:

$$\vec{V}_t = \frac{V_{dc}}{2}\vec{m} \tag{12}$$

Where, $\vec{V}_t$ is the output AC voltage of VSI in space phasor domain, $\vec{m}$ is the modulation index of VSI in space phasor domain, $V_{dc}$ is the input DC voltage of VSI. The dynamics of the DC link voltage of VSI is displayed by the sequent equation [18, 19]:

$$C_{dc}.\frac{dV_{dc}}{dt} = I_{pv} - I_{dc} \tag{13}$$

Where $C_{dc}$ is the DC link capacitance of VSI and $I_{dc}$ is the input DC current of VSI. The input DC current is shown as:

$$I_{dc} = \frac{3(m_d i_{td} + m_q i_{tq})}{4} \tag{14}$$

Where $m_d$ and $m_q$ are the modulation index in d-q frame, $i_{td}$ and $i_{tq}$ are the output currents of inverter in d-q frame. The output of VSI is filtered using a low pass LC filter and joined to the distribution network by a Star/Delta coupling transformer [7]. Filter inductance $L_f$ and filter capacitance $C_f$ and the coupling transformer are modelled as an ideal transformer in series with its leakage inductance $L_r$. The nonlinear state equations of the entire PV, filter, coupling transformer and current controller are given by Eqs. (15)-(29):

$$L_f \frac{di_{td}}{dt} = -R_f i_{td} + u_d + V_{cfd} \tag{15}$$

$$L_f \frac{di_{tq}}{dt} = -R_f i_{tq} + u_q + V_{cfq} \tag{16}$$

$$\frac{dV_{cfd}}{dt} = \frac{i_{td}}{C_f} + \omega V_{cfq} - \frac{i_{sd}}{2\pi f \omega C_f} \tag{17}$$

$$\frac{dV_{cfq}}{dt} = \frac{i_{tq}}{C_f} + \omega V_{cfd} - \frac{i_{sq}}{2\pi f \omega C_f} \tag{18}$$

$$\frac{dx_1}{dt} = Ki_1(P_{ref} - P) \tag{19}$$

$$\frac{dx_2}{dt} = Ki_2(Q_{ref} - Q) \tag{20}$$

$$\frac{dx_3}{dt} = Ki_3(i_{tdref} - i_{td}) \tag{21}$$

$$\frac{dx_4}{dt} = Ki_4(i_{tqref} - i_{tq}) \tag{22}$$

$$i_{tqref} = Kp_1(P_{ref} - P) + x_1 \tag{23}$$

$$i_{tdref} = Kp_2(Q_{ref} - Q) + x_2 \tag{24}$$

$$u_d = Kp_3(i_{tdref} - i_{td}) + x_3 \tag{25}$$

$$u_q = Kp_4(i_{tqref} - i_{tq}) + x_4 \tag{26}$$

For decoupling and linearizing the dynamics, the control inputs $m_d$ and $m_q$ are defined foundation on the following control laws [18]:

$$m_d = \frac{V_{dc}}{2}(V_{cfd} + u_d - \omega_0 i_{tq} L_f) \tag{27}$$

$$m_q = \frac{V_{dc}}{2}(V_{cfq} + u_q + \omega_0 i_{td} L_f) \tag{28}$$

Here, $u_d$ and $u_q$ are the novel control inputs and are substituted into Eqs. (27)-(28).

The DC-Link Voltage Controller certify which $V_{dc}$ is maintained at $V_{dcref}$ so that, the corresponding active power gets delivered from the PV system to the grid. This relation is governed by the following power balance equation:

$$\frac{d}{dt}\left[\frac{C_{dc}V_{dc}^2}{2}\right] \cong P_{PV} - P_{VSI} \tag{29}$$

Eqs. (17)-(22) constitute state space model for controller subsystem. The pursuit are state variables, inputs and outputs:

State Variables: $[x_1, x_2, x_3, x_4, V_{dc}, i_{td}, i_{tq}]$

Inputs: $[V_{cfd}, V_{cfq}, i_{td}, i_{tq}]$

Outputs: $[m_d, m_q]$

A complete PV plant controller is shown in Fig. 3. According to this figure, the sub-synchronous resonance mitigation is obtained by an additional SSRDC on either the active power control loop (active power modulation) or the reactive power control loop (reactive power modulation). The SSRDC structure and design process will be explained in the next section.

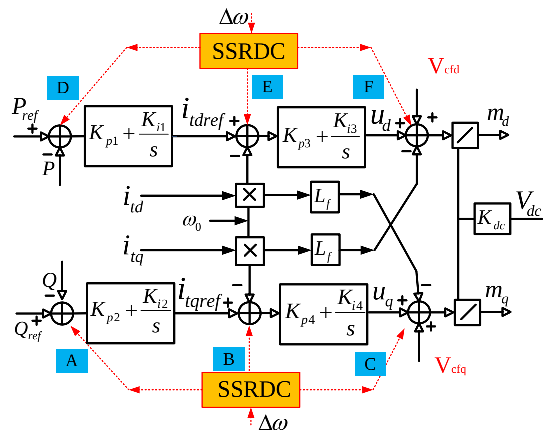


Fig. 3. Photovoltaic controller.

## 3. Whale Optimization Algorithm (WOA)

### 3.1. Introduction

Whale optimization algorithm is a meta-heuristic algorithm that was introduced by Mirjalili in 2016. The algorithm is an inspiration by hunting humpback whales behaviour. Whales are the greatest mammals in the world. They are mostly predators and the important point about them is that they are very smart and emotional animals [20]. Also, it has been demonstrated that a whale is able to think, learn, judge, communicate, and rather has a sentimental relationship. The humpback whale's hunting method is so that after observing a fish school or krill, they produce bubbles through a specific method. The bubbles are in spiral form and go upside, where fish schools and krill are trapped inside the bubbles. This kind of hunting is unique and belongs to humpback whales. Mathematical modelling of the whale algorithm resulted from encircling the prey through circular bubblers, feeding manoeuvre and search for prey are explained below.

### 3.2. Encircling prey

Humpback whales identify the prey place and then besiege them. Because the optimum location is in the search area and it is not predictable, WOA algorithm considers the best current candidate solution as the target prey or assumes that it is near to the optimum. At next step, since the search agent is specified, the other search agents update their locations towards the best search agent. This manner is expressed by the pursuit equations [20]:

$$\vec{D} = \left|\vec{C}.\vec{X}^*(t) - \vec{X}(t)\right| \tag{30}$$

$$\vec{X}(t+1) = \vec{X}^*(t) - \vec{A}.\vec{D} \tag{31}$$

Where $t$ is the current iteration, $A$ and $C$ are coefficient vectors, $X^*$ is the best location vector achieved so far, $X$ is the position vector, $|\ |$ is the absolute value and $\cdot$ is an element by element multiplication. It should be noted that here $X^*$ should be updated in each iteration and the better solution must be chosen. $A$ and $C$ vectors are obtained as [20]:

$$\vec{A} = 2\vec{a}\ .\ \vec{r} - \vec{a} \tag{32}$$

$$\vec{C} = 2\ .\ \vec{r} \tag{33}$$

$\vec{a}$ is a linearly decreasing vector from 2 to 0 during the iteration period (in both exploration and exploitation phases) and $\vec{r}$ is a random vector in the range of [0, 1].

### 3.3. Bubble-net attacking method (Exploitation phase)

For getting mathematical model of the bubble-net behaviour of humpback whales, the following ways have been obtained:

Shrinking mechanism of encircling: To achieve the behavior the value of $\vec{a}$ in Eq. (32) is decreased. It must be noted that the variation span of $\vec{A}$ is reduced by $\vec{a}$. It means that the value of $\vec{A}$ is random in the range of [-a, a], where a is reduced from 2 to 0 during the repetition. Tuning the random values for $\vec{A}$ is in the range of [-1, 1], where the novel situation is defined through a search factor at each point located among the main situation of the agent and the best situation of the current agent.

Spiral updating position: the first way for calculating the distance among the whale and the prey placed in two positions respectively is a spiral equation formed among the positions of the whale and the prey. Imitating the spiral-shape humpback whale movement is given as [20]:

$$\vec{X}\,(t+1) = \vec{D'}\,.e^{bl}\;.\cos\left(2^{\pi} l\right) + \vec{X^*}\,(t) \tag{34}$$

It should be noted that humpback whales swim around the prey in a shrinking circle way and a spiral way at the same time. The mathematical model is explained as below [19]:

$$\vec{X}\,(t+1) = \left\{ \begin{array}{ll} \overrightarrow{X^*}\,(t) - \vec{A}\,.\,\vec{D} & if \;\; p < 0.5 \\ \vec{D'}\;\,.\,e^{bl}\;.\;\;\cos\left(2l\right) + \overrightarrow{X^*}\,(t) & if \; p > 0.5 \end{array} \right\} \tag{35}$$

### 3.4. Prey searching (Exploration phase)

This approach could be employed for searching prey (exploration) based on the vector variety. As a matter of fact, humpback whale randomly searches according to the position. So, using random amount larger than 1 and less than -1, the search agent is forced to move far away from a reference whale. In contrast to the exploitation phase, situation of a search agent in exploitation phase is randomly updated pursuant to the search agent, and is selected as the best search agent. The mathematical model is explained as [20]:

$$\vec{D} = \left|\vec{C}\;.\;X_{\vec{rand}} - \vec{X}\right| \tag{36}$$

$$\vec{X}\,(t+1) = X_{\vec{rand}} - \vec{A}\;.\;\vec{D} \tag{37}$$

Where, $x_{\vec{rand}}$ is the random situation vector. The pseudo code and flowchart of WOA algorithm are shown in Figs. 4 and 5 respectively.

## 4. SSR DAMPING CONTROLLER DESIGN

A conventional lead-lag damping controller used in power system content is adapted for damping the system swings [21]. The damping controller is given in Fig. 6 and consists of a gain block, a washout filter and two lead-lag compensators. The damping controller is planned so as to usually a supplementary electrical torque in phase with the speed deviation to increase the damping of system swings [21].

The Photovoltaic subsidiary damping controller fulfils the rotor speed deviations ($\Delta\omega$) as a feedback signal to produce the extra damping signal. It is accepted that the input signal for damping controller playact a main duty in stabilizing the power system oscillations [5, 6]. In addition, it has been shown that the generator rotor speed includes nearly all of the oscillatory modes of the system and in most published literatures in this issue, the generator rotor speed deviations are used as damping controller input signal [3], [8], [11, 12] and [21]. Thus, in the current paper, the $\Delta\omega$ is fulfilment as a feedback signal in an auxiliary damping controller as it is given in Fig. 6. Another fundamental topic in planning a damping controller for a photovoltaic farm is choosing a suitable spot for inserting damping controller output signal for damping of oscillation. The selection of an appropriate control loop and the choice of a suitable point for applying damping controller can greatly increase damping performance of designed damping

```
Initialize the whales population Xi (i = 1, 2, ..., n)
Calculate the fitness of each search agent
X*=the best search agent
while (t < maximum number of iterations)
    for each search agent
      Update a, A, C, l, and p
        if1 (p<0.5)
          if2 (|A| < 1)
            Update the position of the current search agent by the Eq. (31)
          else if2 (|A|
            Select a random search agent (Xrand )
            Update the position of the current search agent by the Eq. (37)
        end if2
      else if1 (p 0.5)
          Update the position of the current search by the Eq. (34)
      end if1
    end for
    Check if any search agent goes beyond the search space and amend it
    Calculate the fitness of each search agent
    Update X* if there is a better solution
    t=t+1
end while
return X*
```

Fig. 4. Pseudo code of WOA algorithm [20].

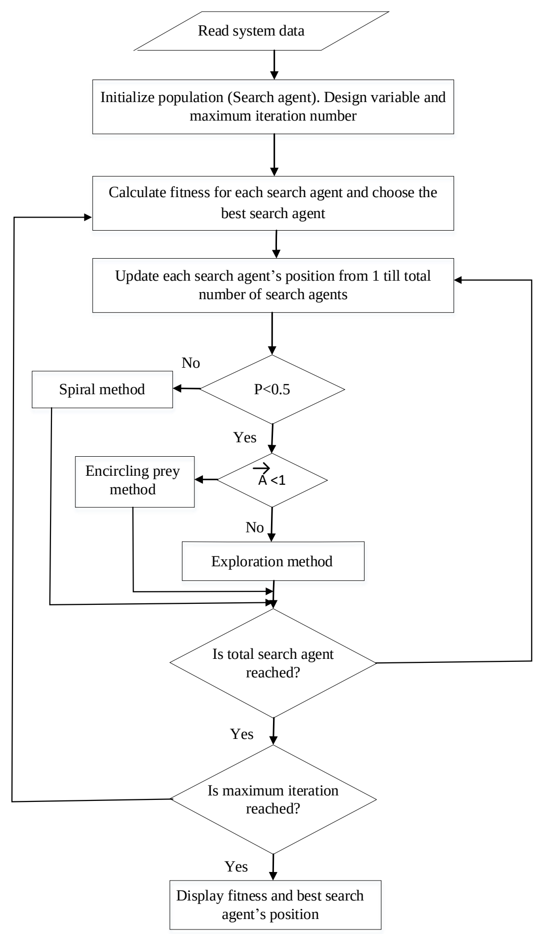


Fig. 5. The flowchart of WOA algorithm.

Table 1. Eigenvalues analyses of the FBM system without PV.

| Mode | Compensation of 26.5% | Compensation of 41.1% | Compensation of 54.7% | Compensation of 68.5% |
|---|---|---|---|---|
| 5 | -0.49± 298.28i | -0.49± 298.28i | -0.49± 298.28i | -0.49± 298.28i |
| 4 | **1.19± 203.0i** | 0.10± 202.83i | -0.11± 202.90i | -0.11± 202.94i |
| 3 | -0.44± 160.58i | **-0.95± 160.67i** | -0.43± 160.50i | -0.44± 160.58i |
| 2 | -0.14± 127.02i | -0.14± 127.09i | **-0.59± 127.13i** | -0.14± 126.99i |
| 1 | -0.22± 98.76i | -0.21± 99.38i | -0.18± 99.88i | **4.50± 98.97i** |
| 0 | -0.44± 8.39i | -0.50± 9.26i | -0.59± 10.28i | -0.73± 11.62i |
| Sub-synchronous | **-4.45± 203.27i** | **-3.90± 160.8i** | **-2.50± 127.29i** | **-5.38± 98.94i** |

controllers. It can be seen from Fig. 3 the sub-synchronous resonance damping controller can be employed at different spots of the photovoltaic plant's active and reactive power controllers, named as A–C and D–F respectively. In the next sections, these points are tested to realize where the SSRDC could be inserted.

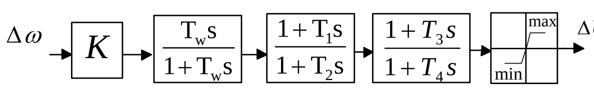


Fig. 6. SSR damping controller block diagram.

## 5. Simulation Results and Eigenvalues Analysis

### 5.1. Simulation results and eigenvalue analysis without PV plant

In this section, first, eigenvalues analysis of the FBM system is expressed without PV plant. In the following nonlinear simulation for both test systems will be expressed without PV plant. For eigenvalue analysis, the system under study has been investigated in four levels of compensation. The eigenvalues analysis for the four compensation levels is presented in Table 1. For getting the eigenvalues, dynamic equations for the whole system were written in form of state space equations and linearized at the system's operating point. As shown in Table 1, due to the small distance between torsional modes' frequency and sub-synchronous mode's frequency, torsional modes were unstable. As a result, the amplitude of the oscillation increases after a short time, causing damage to the generator's mechanical part.

For simulation studies, the performance of the both studied systems (FBM and SBM) are investigated without PV plant. In both systems, the contingency simulated is a three-phase-to-ground fault (shown in Fig. 1) that starts at t= 2 sec. and lasts for 75 msec. In current instance, series compensation level for FBM system is set to 68.5% and for SBM is tune to 55%. Because of the selected amount of series capacitor, when the fault is cleared, large oscillations will be happened between the different sections of the turbine-generator shaft. Fig. 7 (a-b) show the time responses of generator rotor speed deviations ($\Delta\omega$) during and after clearing fault, for system I and II respectively. As it could be shown from the figures, in both systems the turbine-generator shaft show intensive sub-synchronous resonance instabilities.

### 5.2. Simulation results and eigenvalue analysis with PV plant equipped to SSRDC

As mentioned earlier, the IEEE first and second benchmark models (shown in Fig. 1) are extracted as two test systems.

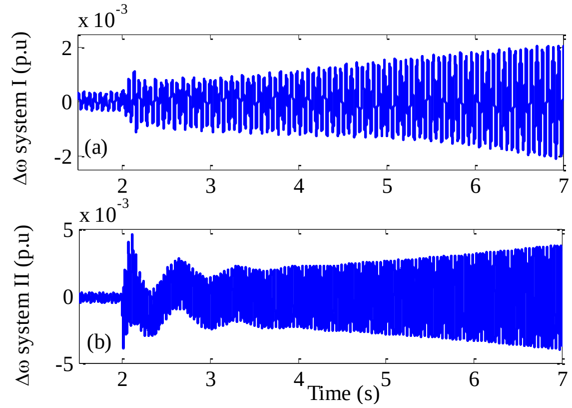


Fig. 7. Time responses of test systems rotor speed deviations ($\Delta\omega$) without PV plant. (a) System I, (b) System II.

Table 2. Eigenvalues analyses of the FBM system with PV and SSRDC.

| Mode | Compensation of 26.5% | Compensation of 41.1% | Compensation of 54.7% | Compensation of 68.5% |
|---|---|---|---|---|
| 5 | -0.72± 298.28i | -0.72± 298.28i | -0.72± 298.28i | -0.68± 298.28i |
| 4 | **-0.02± 203.69i** | -0.12± 202.42i | -0.14± 202.76i | -0.14± 202.85i |
| 3 | -0.63± 160.81i | **-0.58± 161.13i** | -0.55± 159.54i | -0.6± 160.45i |
| 2 | -0.16± 127.08i | -0.16± 127.11i | **-0.15± 127.18i** | -0.1± 126.64i |
| 1 | -0.29± 99.44i | -0.28± 99.63i | -0.27± 99.92i | **-0.21± 100.86i** |
| 0 | -0.48± 10.51i | -0.57± 11.14i | -0.64± 11.87i | -0.68± 12.01i |
| Sub-synchronous | **-2.25± 219.11i** | **-1.91± 181.34i** | **-1.59± 152.19i** | **-1.09± 119.95i** |

The analysis with SSRDC can be performed based on eigenvalue analysis and transient simulation but, due to the multiplicity of studied cases and high value of simulation results, in this part, simulation results and eigenvalue analysis for first benchmark systems will be provided and in the next sections just the second benchmark simulation results will be provided. Also, in the whole simulations, results given in this study are as follows:

- In both study systems, the contingency is a three-phase-to-ground fault at bus 2 (shown in Fig. 1) that happens at t= 2 sec. and hangs on for 75 msec., that the system is unstable without SSRDC, because of the SSR mode.
- In all sections, the SSRDC parameters in the simulation are obtained using WOA algorithm, as mentioned before.

#### *A) Simulation results and eigenvalue analysis for first benchmark test system*

Fig. 8 shows the time responses of first benchmark test systems rotor speed deviations and machine electrical torque during and after clearing fault at bus 2 when the SSRDC is carried out at point A (see Fig. 3). As shown in this figure, the rotor speed deviations before the fault is zero. After clearing the fault, the sub-synchronous oscillations increases for a few seconds. Then, the PV plant slowly controls these oscillations to zero. Therefore, the turbines of the generator shaft will still experience swings because of the perturbation in the system, but they will be damped and slowly go back to the pre-fault value as shown in Fig. 8. It can be shown from Fig. 8-(b) that the maximum peak torque is equal to 1.5 p.u. Although, the duration is only for a few cycles so, there is no risk for the generator shaft.

The eigenvalues of the first benchmark test system, when the SSR damping controller is inserted at point A are displayed in Table 2. Comparing the eigenvalue results without PV plant

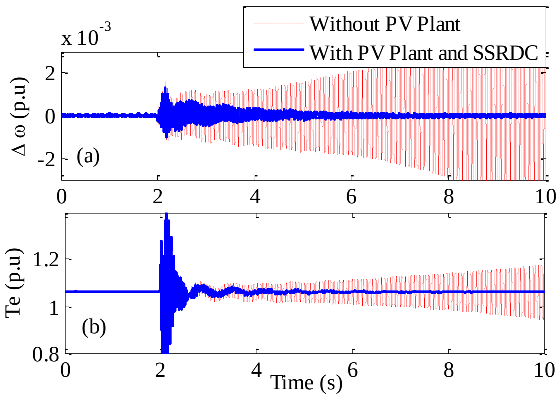


Fig. 8. Time responses of study system I (first benchmark test system) (a). Rotor speed deviations ($\Delta\omega$) (b). Machine electrical torque ($T_e$) with and without SSRDC.

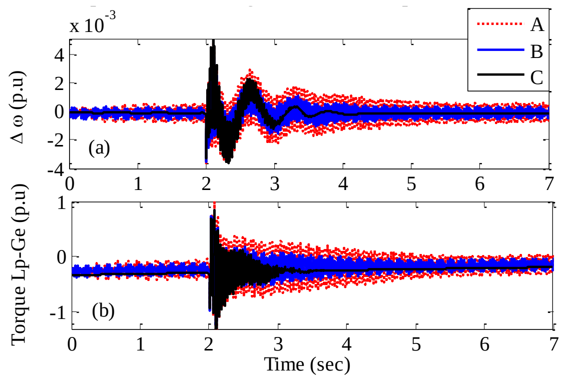


Fig. 9. Time responses of second benchmark system when SSRDC applied at points A, B and C. (a) Rotor speed deviations ($\Delta\omega$) (b) The torque between generator and low pressure turbine.

equipped to SSRDC (refer Table 1), the subsequent results can be reached. The positive values of real part of eigenvalues in Table 1 have been changed to negative ones because, the sub-synchronous damping controller is able to mitigate all the torsional swings on the generator shaft.

1) The damping of critical mode-2 has mainly progressed with SSRDC.
2) The damping of all torsional modes is rises up with SSRDC.
3) Mode-5 is not affected because its modal inertia is very high.
4) The damping of sub-synchronous network mode is decreased with SSRDC.

### *B) SSRDC implemented in reactive power control loop (points A, B and C) for second benchmark test system*

As it can be seen from Fig. 3, the SSRDC can be implemented at several points of the photovoltaic plant's active and reactive power controllers, identified as A–C and D–F. In current section, simulation scurvies are implemented to find out the best location PV plant of active and reactive power controllers for applying SSRDC with the goal of getting the best damping. As said earlier, due to the multiplicity of studied cases and the high value of simulation results, just in one section (Subsection 5.1), simulation results and eigenvalue analysis for first benchmark systems have been provided and in following sections, just the second benchmark simulation results will be provided. Fig. 9 shows the time responses of second benchmark test systems rotor speed deviations and shaft torsional torques among and after clearing fault at bus 2, where the sub-synchronous resonance damping controllers is employed at points A, B, and C. It can be concluded from these figure that implementing the SSRDC at point C gives superior implementation compared to inserting the SSRDC at points A and B in terms of settling time.

### *C) SSRDC implemented in active power control loop (points D, E and F) for second benchmark test system*

This section evaluates the effectiveness of the SSRDC implementation at different points of PV plant's active power control loop, identified in Fig. 3 as D, E and F in mitigating the SSR. Fig. 10 (a and b) displays the time responses of second benchmark test systems rotor speed deviations and shaft torsional torques among and after clearing fault at bus 2, when the SSRDC is inserted at points D, E, and F. It can be seen from this figures that inserting the SSRDC at all three points of PV plant's active power control loop could damp the SSR and stabilize the system. But it is quite clear that implementing the SSRDC at point E leads to slightly better implementation compared to inserting the SSRDC at points D in terms of settling time and also the best possible damping is achieved when the SSRDC is applied at point F. This shows that the SSRDC can interchangably be implemented at points D, E, and F. In addition, Fig. 11 (a and b) compares the photovoltaic farm's active and reactive power with the SSRDC inserted at point D, E and F. The figure displays which performance of the SSRDC at points E and F causes much less settling time in photovoltaic plant's active and reactive power compared to when the SSRDC is inserted at point D. It means that insertion of the SSRDC at E and F is a better option measure to D.

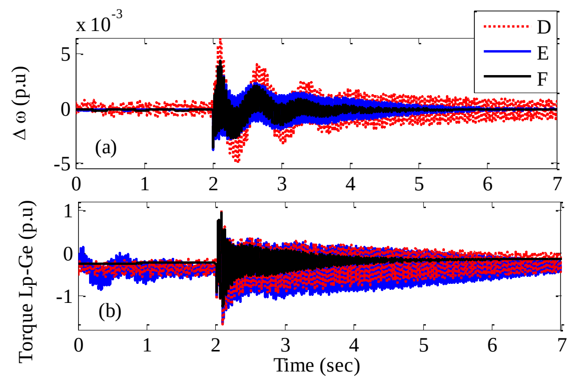


Fig. 10. Time responses of second benchmark system when SSR damping controller applied to points D, E and F. (a) Rotor speed deviations ($\Delta\omega$) (b) Torque belong generator and low pressure turbine.

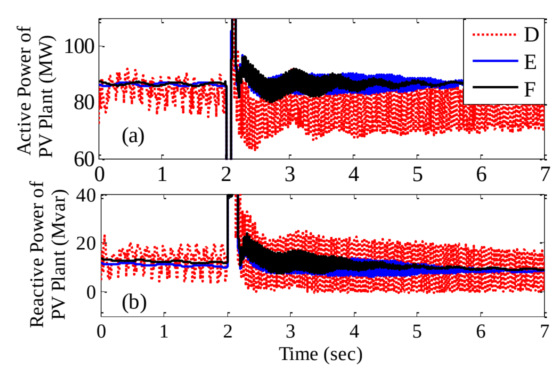


Fig. 11. Time responses of PV plant output active and reactive power when SSRDC applied at points D, E and F. (a) PV plant active power (b) PV plant reactive power.

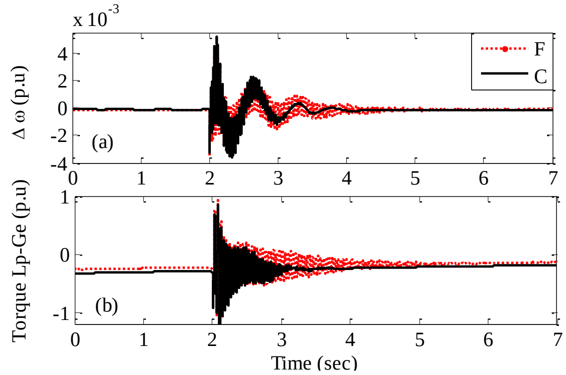


Fig. 12. Time responses of second benchmark system when SSRDC applied at points C and F. (a) Rotor speed deviations ($\Delta\omega$) (b) Torque between generator and low pressure turbine.

Table 3. Performance index calculation for different applied points.

| **Case** | $PI_1$ | $PI_1$ |
|---|---|---|
| **A** | 11.4 | 0.312 |
| **B** | 10.1 | 0.141 |
| **C** | 8.8 | 0.042 |
| **D** | 11.8 | 0.347 |
| **E** | 9.6 | 0.126 |
| **F** | 9.1 | 0.048 |

### *D) Optimal point for SSRDC implementation active and reactive power controller*

In this section the result of simulations for the best point of active and reactive power photovoltaic controller plant (points F and C respectively) are compared to determining of the appropriate control loop and choice of proper point for applying SSRDC.

Fig. 12 (a and b) displays the time responses of second benchmark test systems rotor speed deviations and shaft torsional torques among and after clearing fault at bus 2, when the SSRDC is appended at points C and F. It can be seen from these figures that inserting the SSRDC at both points gives superior performance on damping of oscillations but, the best possible damping is achieved when the SSRDC applied at spot C. These figures displays that performance of the SSRDC at points C creats less settling time in synchronous generator rotor speed deviations and shaft torsional torque compared to when the SSRDC is inserted at spot F. On a technical presentation, both active and reactive power modulation of photovoltaic farm could efficiently raise the oscillations damping but, the function of SSRDC on reactive power control loop represents a better damping in comparison with performance of SSRDC on PV plant active power control loop.

In practical applications, while control of damping is based on real power modulation, renewable energy source commonly has to shorten its real power output. because the value of real power that could be delivered from such sources at any time refers to the environmental situations, so the owner wants to deliver maximum available power. İn addition, if the reactive power modulation is applied, damping of the critical mode increases with the power flow through the transmission line and injected power from renewable energy sources. From the discutions and simulation results, it could be concluded that the spot C at reactive power control loop is the best place to apply the SSRDC.

## 6. Performance Indexes

In order to find appropriate control loop and choose the proper point for implementing damping controller output signal, two Performance Indexes (PIs) are defined on a basis of the system dynamics [22, 23]. These two performance indexes which reflect the settling time and overshoots can be defined as two separate objective functions for each point of photovoltaic plant controllers (A, B, C, D, E, F). For all points (A- F), SSRDC parameters will be optimized with WOA algorithm and then the performance index will be calculated. If one of the performance index has the lower value with one of the spots, that point is the best choice for applying SSRDC and would work effectively and would mitigate the swings rapidly. These two performance indexes are shown as:

$$\mathrm{PI}_1 = \int_0^{t_{sim}} t.(|T_{GE-LP}| + |T_{LP-HP}|)dt \qquad (38)$$

$$PI_2 = 10^3 \int_0^{t_{sim}} (t.\Delta\omega)^2 dt \qquad (39)$$

Where, $t_{sim}$ is the simulation time, $\Delta\omega$ is the speed deviation of the generator rotor speed, $T_{GE-LP}$ is the torque among generator and low pressure turbine and $T_{LP-HP}$ is the torque among low pressure and high presure turbinees. The PI calculations for all cases are shown in Table 3. It is revealed that the lowest calculated PI for reactive control loop is for point C and the lowest calculated PI for active control loop is for point F. Also, it can be seen that the minimum calculated PI values are for point C. Like simulation results, these results also demonstrates the settling time and speed deviations of the generator rotor which majorly increased by insering the suggested damping controller to reactive power control loop of photovoltaic plant.

## 7. CONCLUSION

In this article, SSR damping using modulation of active and reactive power in a high penetration photovoltaic farm is investigated. To investigate this , the IEEE first and second benchmark models are used for computer simulation of sub-synchronous resonance. At first, the simulation model and modal analysis (eigenvalue analysis) are performed for a high penetration PV plant aggregated with a series compensated electric system in MATLAB/Simulink. Then, for damping SSR, a WOA based conventional SSRDC is planned and combined to the original control loop of photovoltaic plant. Simulation results and eigenvalue analysis for study systems showed that proposed SSRDC could efficiently damp the sub-synchronous resonance. In the following, to determine the PV plant best control loop and optimum point for applying SSRDC, the WOA based SSRDC has been designed and added to all points of active and reactive control loops of PV plant (see Fig. 3). The simulation results and two performance indexes (PIs) that show the settling time and overshoots have been used to identify the best control loop and best point to apply SSRDC. Briefly, the following results could be extract regarding the optimum control loop and proper point.

1) For reactive power modulation, implementing the SSRDC at point C gives the best performance compared to inserting the SSRDC at points A and B.
2) For active power modulation, implementing the SSRDC at point F gives the best performance compared to inserting the SSRDC at points D and E.
3) Comparisons of simulation results and PI analysis among active and reactive power modulation showed that both active and reactive power modulation of photovoltaic plant can effectively enhance the damping of the sub-synchronous resonance. So, the operation of SSRDC on reactive power control loop provides a better damping in comparison with the implementation of SSRDC on PV plant active power control loop.

## References


[1] A. Husham, I. Kamwa, M. A. Abido, and H. Suprême, "Decentralized stability enhancement of dfig-based wind farms in large power systems: Koopman theoretic approach," *IEEE Access*, vol. 10, pp. 27684–27697, 2022.

[2] Y. Zhou, L. Qin, and Y. Li, "Output-feedback photovoltaic wadc by h criterion using auxiliary function," *Int. J. Electr. Power Energy Syst.*, vol. 136, p. 107603, 2022.

[3] S. Mehri, M. Shafie-Khah, P. Siano, M. Moallem, M. Mokhtari, and J. Catalão, "Contribution of tidal power generation system for damping inter-area oscillation," *Energy Convers. Manage.*, vol. 132, pp. 136–146, 2017.

[4] Y. Bostani and S. Jalilzadeh, "A new approach based on wide-area fuzzy controller for damping of sub synchronous resonance in power system including dfig," *J. Oper. Autom. Power Eng.*, vol. 11, no. 1, pp. 61–68, 2023.

[5] M. E. Bento and R. A. Ramos, "Selecting the input-output signals for fault-tolerant wide-area damping control design," in *2021 IEEE Texas Power Energy Conf.*, pp. 1–5, IEEE, 2021.

[6] S. Jayakrishnan, E. P. Cheriyan, and T. Sindhu, "Best input—location pair selection for ssr damping controller in dfig based wind farms," *IEEE Access*, vol. 9, pp. 160332–160346, 2021.

[7] H. A. Mohammadpour and E. Santi, "Ssr damping controller design and optimal placement in rotor-side and grid-side converters of series-compensated dfig-based wind farm," *IEEE Trans. Sustainable Energy*, vol. 6, no. 2, pp. 388–399, 2015.

[8] R. K. Varma and M. Akbari, "Simultaneous fast frequency control and power oscillation damping by utilizing pv solar system as pv-statcom," *IEEE Trans. Sustainable Energy*, vol. 11, no. 1, pp. 415–425, 2019.

[9] A. Nateghi and H. Shahsavari, "Optimal design of fpiˆ $\lambda$ dˆ $\mu$ based stabilizers in hybrid multi-machine power system using gwo algorithm," *J. Oper. Autom. Power Eng.*, vol. 9, no. 1, pp. 23–33, 2021.

[10] H. Maleki and R. K. Varma, "Coordinated control of pv solar system as statcom (pv-statcom) and power system stabilizers for power oscillation damping," in *2016 IEEE Power Energy Soc. Gener. Meet.*, pp. 1–5, IEEE, 2016.

[11] M. Khayyatzadeh and R. Kazemzadeh, "Sub-synchronous resonance damping using high penetration pv plant," *Mech. Syst. Signal Process.*, vol. 84, pp. 431–444, 2017.

[12] R. K. Varma and R. Salehi, "Ssr mitigation with a new control of pv solar farm as statcom (pv-statcom)," *IEEE Trans. Sustainable Energy*, vol. 8, no. 4, pp. 1473–1483, 2017.

[13] I. S. working group *et al.*, "First benchmark model for computer simulation of subsynchronous resonance," *IEEE Trans. Power Appar. Syst.*, vol. 96, no. 5, pp. 1565–1572, 1977.

[14] R. Farmer, "Second benchmark model for computer simulation of subsynchronous resonance ieee subsynchronous resonance working group of the dynamic system performance subcommittee power system engineering committee," *IEEE Power Eng. Rev.*, no. 5, pp. 34–34, 1985.

[15] K. Liao, Z. He, Y. Xu, G. Chen, Z. Y. Dong, and K. P. Wong, "A sliding mode based damping control of dfig for interarea power oscillations," *IEEE Trans. Sustainable Energy*, vol. 8, no. 1, pp. 258–267, 2016.

[16] K. Padiyar, "Power system dynamics: stability and control," *Interline, Bangalore*, 1996.

[17] L. Fan, C. Zhu, Z. Miao, and M. Hu, "Modal analysis of a dfig-based wind farm interfaced with a series compensated network," *IEEE Trans. Energy Convers.*, vol. 26, no. 4, pp. 1010–1020, 2011.

[18] A. Yazdani, A. R. Di Fazio, H. Ghoddami, M. Russo, M. Kazerani, J. Jatskevich, K. Strunz, S. Leva, and J. A. Martinez, "Modeling guidelines and a benchmark for power system simulation studies of three-phase single-stage photovoltaic systems," *IEEE Trans. Power Delivery*, vol. 26, no. 2, pp. 1247–1264, 2010.

[19] Y. Ye, M. Kazerani, and V. H. Quintana, "Modeling, control and implementation of three-phase pwm converters," *IEEE Trans. Power Electron.*, vol. 18, no. 3, pp. 857–864, 2003.

[20] S. Mirjalili and A. Lewis, "The whale optimization algorithm," *Adv. Eng. Software*, vol. 95, pp. 51–67, 2016.

[21] P. Kundur, "Power system stability," *Power Syst. Stab. Control*, vol. 10, pp. 7–1, 2007.

[22] J. Khazaie, M. Mokhtari, M. Khalilyan, and D. Nazarpour, "Sub-synchronous resonance damping using distributed static series compensator (dssc) enhanced with fuzzy logic controller," *Int. J. Electr. Power Energy Syst.*, vol. 43, no. 1, pp. 80–89, 2012.

[23] H. Shayeghi, H. Shayanfar, S. Jalilzadeh, and A. Safari, "Design of output feedback upfc controller for damping of electromechanical oscillations using pso," *Energy Convers. Manage.*, vol. 50, no. 10, pp. 2554–2561, 2009.